Analyst

ROYAL SOCIETY OF CHEMISTRY

MINIREVIEW

View Article Online
View Journal | View Issue

Cite this: *Analyst*, 2025, **150**, 3992

Zirconium-carboxylate metal–organic frameworks as stationary phases for chromatographic separation

Hai-Yue Wei,† Sha-Sha Meng,† Jian Zhang, Mo-Han Gu, Ming Xu * and Zhi-Yuan Gu *

Received 27th April 2025,
Accepted 21st July 2025

DOI: 10.1039/d5an00468c

rsc.li/analyst

Zirconium-based metal–organic frameworks (Zr-MOFs) have emerged as highly promising candidates for high-performance chromatographic stationary phases due to their exceptional stability, well-defined porous architectures, and excellent structural tunability. Due to the rich variety of carboxylate linkers and their strong adaptability to coordination flexibility and adjustable backbone rigidity, carboxylate-based Zr-MOFs have more flexible modifiability. The inherent flexibility in modulating both the pore structures and topology of Zr-MOFs enables directional engineering to meet specific application requirements. This includes precise control over porosity, pore environment, and framework stability, thereby achieving targeted and efficient separation of analytes. This review provides a systematic classification of Zr-MOFs and highlights representative examples. Furthermore, this review systematically analyzes the application of Zr-MOFs and Zr-MOF-based composites in various chromatographic separations, including gas chromatography (GC), high-performance liquid chromatography (HPLC), and capillary electrochromatography (CEC).

1 Introduction

Metal–organic frameworks (MOFs) are a subclass of crystalline porous materials characterized by periodic network architectures, which are formed through coordination-driven self-assembly between metal nodes and organic linkers.[1–5] Their precisely engineered frameworks exhibit exceptional structural adjustability, large porosity, and high surface area, positioning MOFs as advanced functional materials for various applications, such as catalysis,[6,7] sensing,[8,9] gas separation,[10,11] and storage.[12,13] The structural engineering of MOFs proceeds through two synergistic approaches. On the one hand, by precisely modulating the metal nodes, organic linker architectures, and coordination connectivity, it is feasible to *in situ* construct MOFs with distinct spatial topologies.[14,15] On the other hand, the post-synthetic modification serves as an efficient approach for introducing diverse functional motifs into the as-synthesized MOFs without affecting the original structures.[16,17] These strategies allow directional engineering of MOFs with targeted properties, thereby fulfilling the precise requirements across diverse application scenarios.

Among all MOFs, zirconium-based MOFs (Zr-MOFs) have garnered significant interest for practical applications because of their excellent stability and structural diversity.[18,19] The variable coordination geometries of Zr-oxo clusters (*e.g.*, 6-, 8-, or 12-connected modes) result in the topological versatility of Zr-MOFs, such as ***fcu***,[20] ***ftw***,[21] ***reo***,[22] ***spn***,[23] ***csq***,[24] and ***scu***[25] topology. Furthermore, linker diversity further amplifies structural complexity, with carboxylate, phosphonate, pyridine-based, and phenolate ligands serving as primary organic linkers.[26] Carboxylate linkers are widely employed due to their adaptable coordination flexibility (*e.g.*, monodentate, bidentate, or bridging modes) and tunable backbone rigidity. The interplay between zirconium cluster connectivity (*e.g.*, node nuclearity, μ-oxo bridging) and linker geometry (*e.g.*, symmetry, functional group orientation) governs the reticular assembly of Zr-MOFs, underpinning their structural predictability and functional versatility.[27] The modular design paradigm facilitates tailored porosity, stability, and host–guest interactions of Zr-MOFs, which are critical for applications.

In carboxylate-based Zr-MOFs, the tetravalent Zr(IV) ion adopts a high oxidation state with high charge density and bond polarization, which results in a strong affinity for oxygen atoms of carboxylate ligands.[19] The robust Zr–O coordination bonds confer exceptional thermodynamic stability and resistance to aqueous and solvated environments, enabling Zr-MOFs to maintain structural integrity across diverse solvents

State Key Laboratory of Microbial Technology, Jiangsu Key Laboratory of Biofunctional Materials, Jiangsu Collaborative Innovation Center of Biomedical Functional Materials, Jiangsu Key Laboratory of New Power Batteries, College of Chemistry and Materials Science, School of Food Science and Pharmaceutical Engineering, Nanjing Normal University, Nanjing 210023, China.
E-mail: guzhiyuan@njnu.edu.cn, mingxu@njnu.edu.cn
† These authors contributed equally.

and under thermal stress.[28] Based on these advantageous characteristics, Zr-MOFs have become efficient stationary phases in chromatographic separations, such as gas chromatography (GC), high-performance liquid chromatography (HPLC), and capillary electrochromatography (CEC). Their superior separation ability results from two key attributes. On the one hand, Zr-MOFs offer various interaction forces for analyte separation and identification.[29,30] The metal nodes within Zr-MOFs contribute to metal affinity, coordination interactions, and electrostatic interactions, while organic ligands provide hydrogen bonding, hydrophilic/hydrophobic interactions, and π–π interactions. On the other hand, the versatile topologies of Zr-MOFs impart variations in pore size, pore shape, and channel connectivity, which directly influence the diffusion pathways and mass transfer processes of analytes.[31,32] Thus, through rational structural design, Zr-MOFs enable precise modulation of both the thermodynamic interactions with analytes and the kinetic diffusion of analytes, which collectively determine the separation resolution and efficiency. This review systematically introduces different carboxylate-based Zr-MOFs and highlights their applications as advanced stationary phases in GC, HPLC, and CEC (Fig. 1 and Table 1). The applications of some Zr-MOF composites in these areas are also included in the discussion.

2. Typical types of carboxylate-based Zr-MOFs

2.1 Three-dimensional carboxylate-based Zr-MOFs

2.1.1 UiO series. The UiO (UiO = University of Oslo) series MOFs, exemplified by UiO-66, UiO-67, and UiO-68, constitute three-dimensional (3D) periodic architectures with ***fcu*** topology that are constructed through directional coordination assembly of zirconium-oxo clusters and bidentate carboxylate linkers. The most representative one, UiO-66, was first developed by Cavka *et al.* in 2008,[20] which consists of a rigid network formed by Zr_6 clusters and terephthalic acid (H_2BDC) through robust coordination bonds.[33] UiO-66 exhibits a dual-pore system composed of octahedral cages (11 Å diameter) and tetrahedral cages (8 Å diameter), interconnected through triangular micropore windows (5–7 Å). The unique coordination chemistry confers UiO-66 with ultrabroad pH tolerance, exceptional thermal endurance, and chemical stability, which originates from the kinetic inertness of Zr–O bonds.[20] For example, UiO-66 maintains framework stability in common organic solvents such as DMF, acetone, benzene, and methanol, and strong acid solutions with pH = 1. In addition, defect adjustability is another typical feature of UiO-66, which can significantly improve its mass transfer performance, active site exposure, and selective adsorption ability by accurately regulating linker defects or cluster defects.[34–37] For example, Cai *et al.*[38] synthesized defective UiO-66 with lauric acid as the modulator, which improved the catalysis efficiency of UiO-66 due to the formation of more exposed Zr sites and hierarchically porous structures by linker defects.

2.1.2 PCN series. The PCN (PCN = porous coordination network) series of Zr-MOFs is constructed through the coordination of Zr–O clusters with polydentate carboxylate linkers.[39] Their nomenclature follows the "PCN-number" system (*e.g.*, PCN-222, PCN-224, PCN-700, and PCN-777), where numbers usually reflect a synthetic order or topological feature. Among them, PCN-222 is the research hotspot due to its unique structural design and multi-functional features.[40] PCN-222, possessing the ***csq*** topology with a one-dimensional (1D) mesoporous channel (about 3.2 nm) and microporous channel (about 1.3 nm), is composed of Zr_6 clusters and tetrakis(4-carboxyphenyl)porphyrin (TCPP). Due to its inherent open channels and ultra-large specific surface area, PCN-222 has become an ideal candidate adsorbent for molecular adsorption, such as

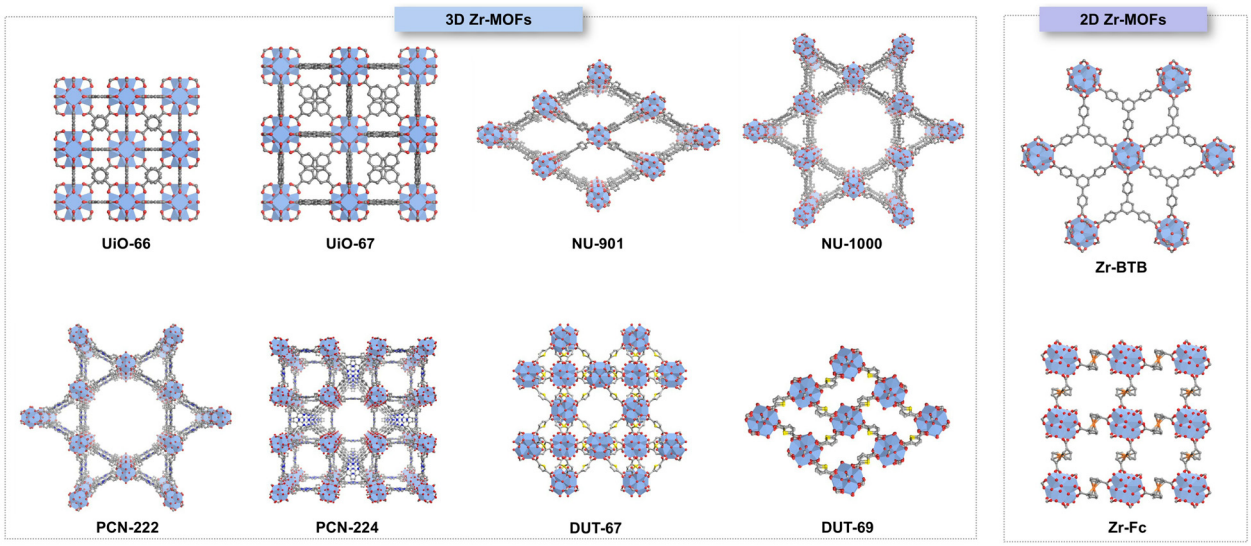

Fig. 1 Schematic of some representative carboxylate-based Zr-MOF structures from different classifications mentioned in this review.

Table 1 Summary of chromatographic separation applications based on carboxylate-based Zr-MOFs and their composites

Zr-MOF material	Analytes	Form	Application	Ref.
UiO-66	Substituted benzene, polycyclic aromatic hydrocarbons	Packing	HPLC	73
DUT-67	Xylene isomers, phthalic acid esters	Packing	HPLC	76
UiO-66@SiO_2 shell-core microspheres (SiO_2-NH_2)	Xylenes, ethylbenzene, alkyl benzenes, anilines	Packing	HPLC	78
UiO-67@SiO_2	Alkylbenzenes, polycyclic aromatic hydrocarbons, anilines, hydrophilic thioureas	Packing	HPLC	79
UiO-66@SiO_2 shell-core microspheres (SiO_2-COOH)	Xylene isomers, substituted benzenes, polycyclic aromatic hydrocarbons	Packing	HPLC	81
MOF-808@SiO_2	Sulfonamides, alkaloids, nucleosides, nucleobases, antibiotic compounds, carbohydrates, amino acid compounds	Packing	HPLC	77
d-MOF-808@SiO_2	Sulfonamides, alkylbenzenes, polycyclic aromatic hydrocarbons	Packing	HPLC	85
Zr-BTB/PDA@silica	Sulfonamides, nucleosides, nucleobases, antibiotic compounds, alkaloids, carbohydrates	Packing	HPLC	84
SSU	Xylene isomers, phenols, aniline, aromatics	Packing	HPLC	82
[BCMIM]Cl-Zr-MOF@SiO_2	Sulfonamides, dinitrobenzenes, iodoanilines	Packing	HPLC	86
CE-MOFs	Amino acids, N-containing drugs	Packing	HPLC	83
MIP-202@SiO_2	Disubstituted benzenes, 1-phenylethanol enantiomers, sulfonamides, nucleosides/nucleobases, B vitamins	Packing	HPLC	80
Fe-CD/MOF@SiO_2	Polycyclic aromatic hydrocarbons, sulfonamides, nucleosides	Packing	HPLC	87
UiO-66	Linear alkanes, alkane isomers, propylbenzene isomers, ethylbenzene, xylene isomers	Dynamic coating	GC	88
PCN-608-N, NU-1000-N	Linear alkanes, alkane isomers, substituted benzenes	Dynamic coating	GC	89
NU-901	Linear alkanes, alkane isomers, ethyltoluene, chlorotoluene isomers	Dynamic coating	GC	90
PCN-608-MOFs, NU-1000-MOFs	Linear alkanes, alkane isomers, substituted benzenes	Dynamic coating	GC	91
CTMOFs	Alkane isomers, substituted benzenes, propylene, propane	Dynamic coating	GC	31
MOSS	Linear alkanes, alkane isomers, substituted benzenes	Dynamic coating	GC	92
UiO-67-3D, UiO-67-2D	Linear alkanes, alkane isomers, substituted benzenes	Dynamic coating	GC	93
Zr-BTB-FA	Linear alkanes, substituted benzenes	Dynamic coating	GC	94
Zr-BTB	Benzene derivative isomers	Dynamic coating	GC	95
Zr-BTB-P-C_x, Zr-BTB-A-C_x (x = 2,3,4)	Substituted benzenes	Dynamic coating	GC	96
Zr-BTB-C_x (x = 2,3,4,5)	Substituted benzenes	Dynamic coating	GC	97
UiO-66-NH_2	Phenoxyacids, phenols, chlorobenzenes	*In situ* growth	CEC	98
NHP-UiO-66	Substituted benzenes, chlorobenzenes, polycyclic aromatic hydrocarbons, nucleosides, polypeptides, basic proteins	Physical coating	CEC	99
Cys-UiO-66	Chlorobenzenes, substituted benzene, halogenated benzenes	Physical coating	CEC	100
Cys-UiO-66-NH_2	Chlorobenzene isomers, selected alkaloids, nonsteroidal anti-inflammatory drugs	Physical coating	CEC	101
Cellulase@poly(GMA-UiO-66-NH_2-EDMA) monolith	Basic and acidic racemic drugs	Monolithic	CEC	102
L-Cys-PCN-224	Natural amino acids	Covalent bonding	CEC	103
L-Cys-PCN-222	Natural amino acids, imidazolinone pesticides, aryloxyphenoxypropionic pesticides, fluoroquinolone drugs	Covalent bonding	CEC	104
L-TRP@MIP(APTES-TEOS)@UiO-66-NH_2@capillary	DL-Tryptophan	Physical coating	CEC	105

chloramphenicol, dye molecules, and perfluorooctane sulfonate.[41–44] Besides, modifying specific functional groups into PCN-222 can effectively improve its adsorption selectivity. For example, Fang *et al.*[45] demonstrated the "Cage-on-MOF" strategy to improve the selective adsorption capacity of PCN-222 to charged dye molecules. By incorporating cages with exposed sulfate and amino groups into the metal sites exposed on PCN-222, the selective adsorption of positively charged methylene blue and negatively charged Eosin Y was increased, respectively.

2.1.3 NU series. NU series Zr-MOFs (NU = Northwestern University) includes NU-1000, NU-901, NU-600, *etc.*[46–48] NU-1000 adopts a ***csq*** topology with 1D hexagonal mesopores (about 3.1 nm) and triangular micropores (about 1.2 nm), which is usually synthesized by adding H_4TBAPy (H_4TBAPy = 1,3,6,8-tetrakis(*p*-benzoic acid)pyrene) to the DMF solution containing $ZrOCl_2 \cdot H_2O$ and modulators under elevated-temperature conditions.[46] The hierarchical porosity of NU-1000, particularly the large amount of mesopores, facilitates rapid molecular diffusion and mitigates mass transport limitations in catalysis. Although the protocol typically yields NU-1000 as the major phase, it is also prone to producing NU-901 with ***scu*** topology and diamond-shaped micropores.[49] The distinct topological structures primarily stem from different orientations of the nodes. Specifically, in NU-1000, the oxo-Zr_6 nodes rotate 120° relative to each other, whereas all nodes are aligned parallelly in NU-901. To obtain phase-pure NU-1000, Webber *et al.*[49] employed a strategy utilizing more rigid 4-phenylbenzoic acid as the modulator, which effectively suppressed the formation of NU-901 impurities due to the strong steric interactions between modulators and misaligned nodes. In order to obtain the pure phase of NU-901, Garibay *et al.*[50]

studied the effects of zirconium salts and carboxylic acid modulators. When employing the non-halogenated zirconium salt $Zr(acac)_4$ in combination with 4-aminobenzoic acid during synthesis, this approach effectively suppressed the formation of the NU-1000 phase while enabling the successful preparation of phase-pure NU-901. Both NU-1000 and NU-901 have application potential in gas selective adsorption and catalysis.[50–53]

2.1.4 DUT series. The DUT (DUT = Dresden University of Technology) series Zr-MOFs are high-performance porous materials that were first developed by Prof. Kaskel *et al.*[54] Typical DUTs, such as DUT-67, DUT-68, and DUT-69, are based on Zr clusters and 2,5-thiophenedicarboxylic acid, forming different crystal structures, topologies, and pore systems.[55] DUT-67 with ***reo*** topology presents two types of microporous cages: cubo-octahedral cage (1.42 nm) and octahedral cage (1.17 nm). The octahedral cages are connected to the cuboctahedral cages through 0.65 nm windows, while the cuboctahedral cages are interconnected *via* 0.85 nm windows. Because of its good chemical stability against water and organic solvents, DUT-67 has been widely applied in water collection and adsorption desalination.[56,57] DUT-68 has a ***bon*** topology, and its cage-typed mesopores can utilize confinement effects to capture gas molecules effectively, making it suitable for capturing carbon dioxide and iodine vapor.[58] DUT-69 has ***bct*** topology, possessing octahedral cages and channels running along one crystallographic direction, which is widely used in catalysis and other fields due to its large pore size and excellent stability.[59,60]

2.2 Two-dimensional carboxylate-based Zr-MOFs

Two-dimensional (2D) Zr-MOFs are typically composed of multiple ultrathin layers, offering large surface areas and more exposed active sites.[61] The layers are connected by van der Waals forces to form a controllable stacking structure. The lamellar architecture demonstrates excellent flexibility and processability, facilitating the fabrication of self-supporting membranes or composite membranes.[62] Besides, the in-plane nanopores shorten molecular diffusion pathways within the 2D layers, thus improving gas or liquid mass transport. Classic examples of 2D Zr-MOFs include Zr-Fc (Fc = 1,1′-ferrocenedicarboxylic acid),[63] Zr-TCA (TCA = 4,4′,4″-nitrilotribenzoic acid),[64] Zr-BTB (BTB = 1,3,5-tri(4-carboxyphenyl)benzene),[65] and Zr-TATB (TATB = 4,4′,4″-(1,3,5-triazine-2,4,6-triyl)tribenzoic acid).[66] Wang *et al.*[67] first synthesized 2D Zr-BTB with the ***kgd*** topology *via* the solvothermal approach. However, the 2D frameworks can penetrate each other vertically, further forming a 3D structure with aligned 1D channels along the [001] direction. To address this interpenetration issue, Hu *et al.*[68] pioneered a modulated hydrothermal synthesis strategy to kinetically suppress the formation of 3D networks and enable fast precipitation of intermediate 2D nanosheets. Crucially, the interlayer spacing and thickness of 2D Zr-BTB can be precisely modulated. For instance, Wang *et al.*[67] synthesized Zr-BTB nanosheets with controllable thickness by adding water or changing the functionalities of the modulators. In addition, Wang *et al.*[69] conducted initial isolation of ultrathin Zr-BTB nanosheets and subsequently attached porphyrin-based carboxylate ligand TCPP to the unsaturated Zr metal sites of Zr-BTB nanosheets by replacing the terminal $-OH^-/H_2O$ groups of Zr_6 clusters, achieving surface modification of Zr-BTB nanosheets. The obtained 2D Zr-MOF is PCN-134-2D, which could be used as an efficient catalyst for artemisinin production.

3. Applications of carboxylate-based Zr-MOFs in chromatographic separation

The unique properties and diverse structures of carboxylate-based Zr-MOFs make them attractive candidates for chromatographic separation. As chromatographic stationary phases, carboxylate-based Zr-MOFs can provide hydrophilic/hydrophobic interactions, hydrogen bonding, π–π stacking, and the molecular sieving effect for the separation of isomers with similar molecular weights, polarities, and boiling points.[70–72] Currently, carboxylate-based Zr-MOFs have presented high separation ability in HPLC, GC, and CEC. A systematic comparison of Zr-MOF-based stationary phases, highlighting their preparation form and separation performance, is detailed in Table 1.

3.1 Application of carboxylate-based Zr-MOFs in HPLC

HPLC is an analytical technique based on liquid phase separation, featuring high separation efficiency, exceptional sensitivity, and broad applicability. Zr-MOFs with excellent resistance to organic solvents, acids, and bases are ideal candidates as stationary phases for HPLC.

3.1.1 Carboxylate-based Zr-MOF packed columns. Due to their good mechanical stability, Zr-MOFs can be directly packed into stainless steel columns for separations. Zhao *et al.*[73] fabricated the UiO-66 packed column *via* slurry packing, and this column successfully separated substituted benzene (SBs) and polycyclic aromatic hydrocarbons (PAHs) in normal-phase and reverse-phase HPLC modes. Specifically, the xylene isomers followed the elution order of *p*X < *m*X < *o*X on the UiO-66 column. Since the pore size of UiO-66 exceeded the molecular size of xylene isomers, all isomers could enter the pores of UiO-66. Compared with *p*X and *m*X, *o*X with the largest molecular size was most compatible with the pore wall of UiO-66, leading to the strongest van der Waals interaction with UiO-66 and the longest retention time. Conversely, *p*X with high symmetry induced a parallel stacking mode, leading to strong π–π interactions between *p*X molecules and consequently the weakest interactions between *p*X and UiO-66.[73–75] Apart from UiO-66, DUT-67 was also employed as the stationary phase using the same packing method by Chen *et al.*[76] The DUT-67 packed column achieved baseline separation of xylene isomers with the elution order of *p*X < *m*X < *o*X based on the same separation mechanism as the UiO-66 packed column.

3.1.2 Carboxylate-based Zr-MOF composite packed columns. Although directly packed Zr-MOF columns have demonstrated good separation ability, the irregular shape and small particle size of some Zr-MOFs cause high packing pressure and low column efficiency.[77] To address these limitations, Zr-MOF@SiO_2 composites were developed as stationary phases for HPLC, leveraging the superior separation ability of Zr-MOFs while benefiting from the excellent packing properties of spherical SiO_2 substrates. Zhang *et al.*[78] synthesized UiO-66@SiO_2 shell-core microspheres through the one-pot synthesis method. In this approach, 5 μm SiO_2 particles terminated with amino groups were used as nucleation seeds and structural scaffolds for the growth of UiO-66 nanocrystals (Fig. 2a and b). The UiO-66 shell could provide the separation forces for analytes, while the mesoporous SiO_2 core could reduce both the packing pressure and mass transfer resistance, ultimately improving the column efficiency. Besides, the amino groups on SiO_2 could also affect the adsorption and separation of analytes on UiO-66@SiO_2 composites. The UiO-66@SiO_2 packed column demonstrated a similar retention preference as the UiO-66 packed column for retaining *o*X last. However, the UiO-66@SiO_2 packed column exhibited a reversed elution order for *m*X *versus* *p*X (Fig. 2e), as the charge repulsion between alkaline *m*X and surface amino groups led to the weakening of the retention of *m*X in this column. This finding highlights the critical role of SiO_2 surface functionality in modulating the separation selectivity of Zr-MOF@SiO_2 composites. Similarly, Li *et al.*[79] prepared UiO-67@SiO_2 composites by *in situ* growth of the UiO-67 metal–organic framework on amino-functionalized 5 μm silica substrates. The UiO-67@SiO_2 packed column demonstrated a mixed-mode separation mechanism integrating hydrophilic interaction liquid chromatography (HILIC) and reversed-phase liquid chromatography (RPLC), achieving rapid and high-resolution separation for both hydrophobic and hydrophilic analytes. In addition, Si *et al.*[77] pioneered the *in situ* growth of MOF-808 on silica spheres using a static self-assembly strategy, where sodium dodecyl benzenesulfonate (SDBS) was introduced to impart a negative surface charge to pristine silica spheres, thereby attaching Zr^{4+} ions at the silica interface through electrostatic

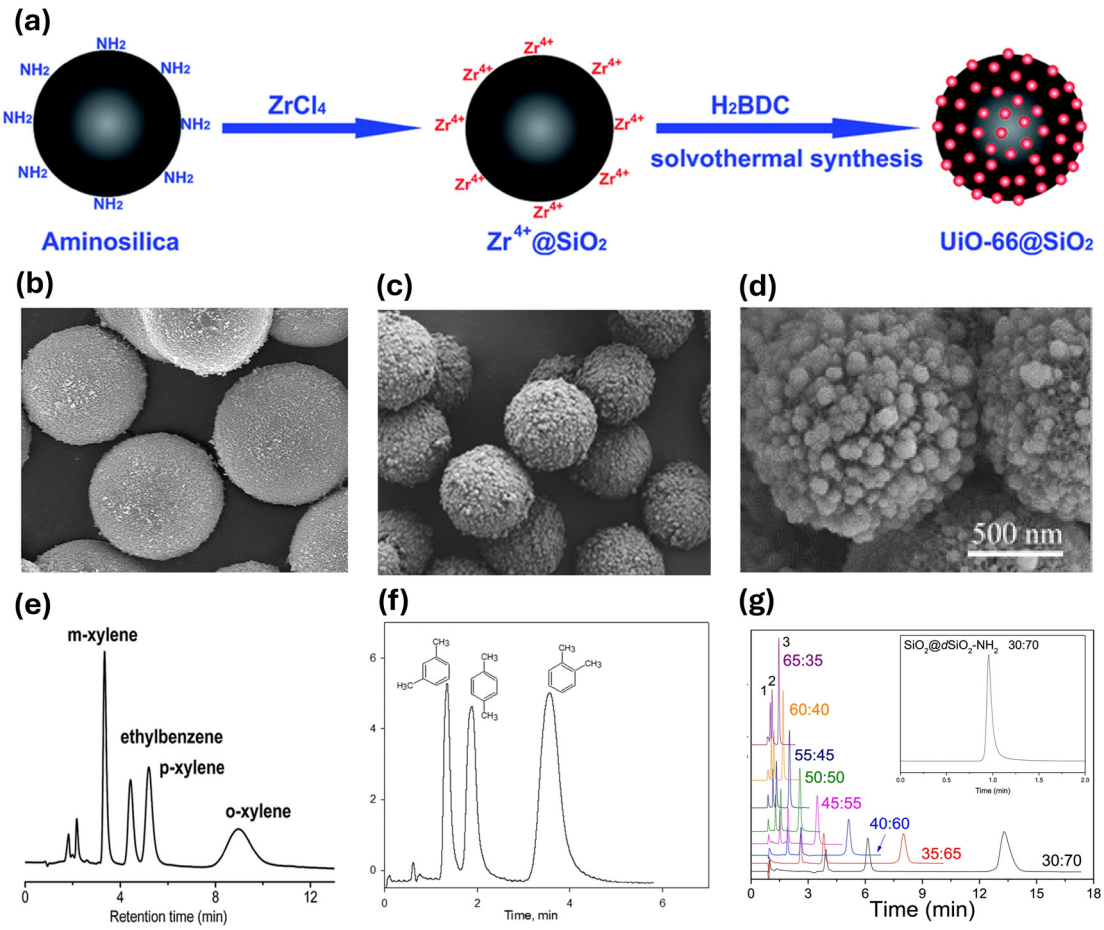

Fig. 2 (a) Synthetic procedure of UiO-66@SiO_2 shell–core microspheres. The SEM images of (b) UiO-66@SiO_2(–NH_2), (c) UiO-66(2×)@SiO_2(5), and (d) SSU-20. Separation of xylene isomers on the (e) UiO-66@SiO_2(–NH_2) column, (f) UiO-66(2x)@SiO_2(5) column, and (g) SSU-20 column [(1) *m*-xylene, (2) *p*-xylene, and (3) *o*-xylene]. (a), (b) and (e) are reproduced with permission from ref. 78. Copyright 2015, The Royal Society of Chemistry. (c) and (f) are reproduced with permission from ref. 81. Copyright 2017, The Royal Society of Chemistry. (d) and (g) are reproduced with permission from ref. 82. Copyright 2023, Elsevier.

interactions. The obtained MOF-808@SiO_2 mainly showed the HILIC retention mechanism, demonstrating exceptional separation efficiency for sulfonamides, alkaloids, nucleosides, nucleobases, antibiotic compounds, carbohydrates, and amino acid compounds, while maintaining robust stability. Compared to the amphiphilic UiO-67@SiO_2 column, the MOF-808@SiO_2 packed column could separate a broader range of hydrophilic compounds.

Recently, Hu *et al.*[80] synthesized MIP-202@SiO_2 composite materials under mild conditions using a hydrophilic deep eutectic solvent (DES) as the reaction medium. MIP-202 was constructed through coordination between zirconium ions and L-aspartic acid. The aspartic acid featured enantioselective recognition sites while polar carboxyl and amino groups conferred hydrophilicity to the MOF. Leveraging the synergistic effects of hydrophilic/hydrophobic, hydrogen bonding, and electrostatic interactions, the MIP-202@SiO_2 composite achieved effective separation of positional isomers, chiral enantiomers, sulfonamides, nucleosides/nucleobases, and B vitamins.

Beyond surface functionality, the porous characteristics of SiO_2 also play a vital role in determining the separation performance of Zr-MOF@SiO_2 packed columns. Arrua *et al.*[81] deposited UiO-66 nanocrystals onto the surface of COOH-modified mesoporous silica (SiO_2(5)-COOH) and non-porous silica (SiO_2(2.1)-COOH) by microwave-assisted solvent synthesis (Fig. 2c). Owing to its higher Brunauer–Emmett–Teller (BET) specific surface area and enriched carboxylic acid functional groups within the shell layer, the UiO-66@SiO_2(5) composite fabricated *via* 5-μm mesoporous silica templating exhibited a denser UiO-66 coating compared to UiO-66@SiO_2(2.1). This structural optimization thereby led to a remarkable improvement in chromatographic separation performance. Notably, when depositing UiO-66 on mesoporous SiO_2(5)-COOH, the resulting UiO-66(2×)@SiO_2(5) packed column exhibited excellent separation ability. This column provided reverse shape selectivity for the separation of positional isomers, where bulkier analytes eluted later due to the stronger van der Waals interactions between bulkier analytes and the pore wall of UiO-66 (Fig. 2f). Wang *et al.*[82] synthesized the metal–organic framework/silica composite (SSU) by growing UiO-66 on the surface of SiO_2 core–shell spheres (SiO_2@dSiO_2) (Fig. 2d). Unlike conventional porous SiO_2 particles, SiO_2@dSiO_2 consisted of non-porous SiO_2 cores and porous SiO_2 shells, offering notable advantages such as uniform particle size and enhanced mass transfer efficiency. The SUU-20 with a spheres-on-sphere structure possessed both the characteristic micropores of UiO-66 (about 1 nm) and mesopores (about 45 nm). Compared to previously reported UiO-66@SiO_2 with micropores, the incorporation of mesopores in SUU-20 effectively reduced the mass transfer resistance of analytes, thereby significantly improving the column efficiency of the SUU-20 packed column (Fig. 2e–g). Notably, the column efficiency of *p*X reached up to 50 452 plates per m.

3.1.3 Functionalized carboxylate-based Zr-MOF composite packed columns. The structural functionality of Zr-MOFs enables the introduction of specific functional groups for the recognition and separation of targets. These tailored functional groups can provide hydrophilicity/hydrophobicity or interaction forces, thereby enhancing separation efficiency. Jiang *et al.*[83] functionalized Zr-MOFs with chiral crown ether moieties through linker functionalization and fabricated chiral stationary phases (CSPs) by mixing the functionalized Zr-MOFs with C18 silica gel. The introduction of chiral crown ether facilitated stereoselective recognition of racemates *via* supramolecular interactions, allowing these CSP-packed columns to exhibit good separation ability for amino acids, amino esters, and racemic drugs. Besides, Si *et al.*[84] modified Zr-BTB with polydopamine (PDA) and composited it with SiO_2 *via* a double-solvent method to obtain the 2D Zr-BTB/PDA@SiO_2 stationary phase for HPLC separation. The hydroxyl and nitrogen-containing groups in PDA could provide hydrophilicity, thereby enhancing the hydrophilic separation performance in chromatography. Furthermore, its benzene rings could strengthen the π–π interaction between Zr-MOF and analytes, improving the separation efficiency of hydrophobic compounds. Although the column efficiency of the 2D Zr-BTB/PDA@SiO_2 packed column was limited due to the pore blockage of SiO_2 caused by PDA and Zr-BTB, this column still exhibited good separation performance for hydrophilic compounds in HILIC mode and for hydrophobic compounds in RPLC mode. Recently, Zhang *et al.*[87] synthesized the Fe-CD/MOF@SiO_2 composite by encapsulating iron metal-doped chiral carbon dots (CDs) in MOF-808. The CDs, synthesized using DL-malic acid as the precursor, not only possessed chiral recognition capability but also featured abundant polar sites, which could significantly enhance hydrogen bonding interactions with analytes. Furthermore, iron ion doping enhanced the acidic functional groups on the CD surface and altered charge distribution, thereby improving separation performance. The resulting Fe-CD/MOF@SiO_2 composite synergistically combined the properties of both MOF-808 and Fe-CDs. This integration led to significantly improved chiral recognition, enhanced hydrophilicity, and stronger hydrogen bonding interactions. Consequently, the composite demonstrated effective separation for diverse analytes, including polycyclic aromatic hydrocarbons, sulfonamides, nucleoside drugs, positional isomers, and enantiomers.

In addition to introducing specific recognition sites and additional forces, post-synthetic modification of Zr-MOFs can adjust the pore structure by modulating defect concentration, thereby enhancing the interactions between analytes and the framework as well as improving the mass transfer of analytes within the pore channels. Si *et al.*[85] synthesized MOF-808 with defects (denoted as d-MOF-808) through post-synthetic modification. The introduction of structural defects enabled precise modulation of the pore architecture of d-MOF-808, transforming the microporous framework into a hierarchical micro-/mesoporous system, thereby optimizing size-selective compatibility with analytes. Compared to the MOF-808@SiO_2 packed column, the d-MOF-808@SiO_2 counterpart demonstrated significantly enhanced separation performance for sulfonamide

antibiotics and alkylbenzenes. This improvement was attributed to the hierarchical pore structure, which synergistically enhanced host–guest molecular interactions and reduced mass transfer resistance, thereby significantly improving separation efficiency.

Furthermore, by rationally functionalizing the Zr-MOF and SiO_2, the stability of the obtained stationary phase can be enhanced obviously. Zhou *et al.*[86] enhanced both the stability and separation ability of Zr-MOF@SiO_2 by modifying it with ionic liquids (ILs, [BCMIM]Cl) (Fig. 3a). On the one hand, the introduction of ILs into the pores of Zr-MOFs reinforced the structural integrity of Zr-MOFs, which bestowed excellent repeatability and stability on the prepared [BCMIM]Cl-Zr-MOF@SiO_2 packed column. Notably, after six months of storage, the separation performance of this column remained unchanged. On the other hand, ILs could enhance multiple interactions between analytes and stationary phases, such as electrostatic interactions, hydrophobic–hydrophilic interactions, and hydrogen bonding.[106] Thus, the [BCMIM]Cl-Zr-MOF@SiO_2 packed column demonstrated superior resolution and separation efficiency for aromatic compounds, sulfonamides, and positional isomers compared to its unmodified Zr-MOF@SiO_2 counterpart (Fig. 3b and c).

3.2 Application of carboxylate-based Zr-MOFs in GC

GC is a widely employed analytical technique for trace separation, characterized by operational simplicity and minimal environmental impact due to solvent-free operation. The stationary phase plays a crucial role in governing chromatographic separation performance. Recently, carboxylate-based Zr-MOFs with diverse structures, tunable pore architectures, and high thermal stability have aroused great attention as the stationary phase for GC separations.

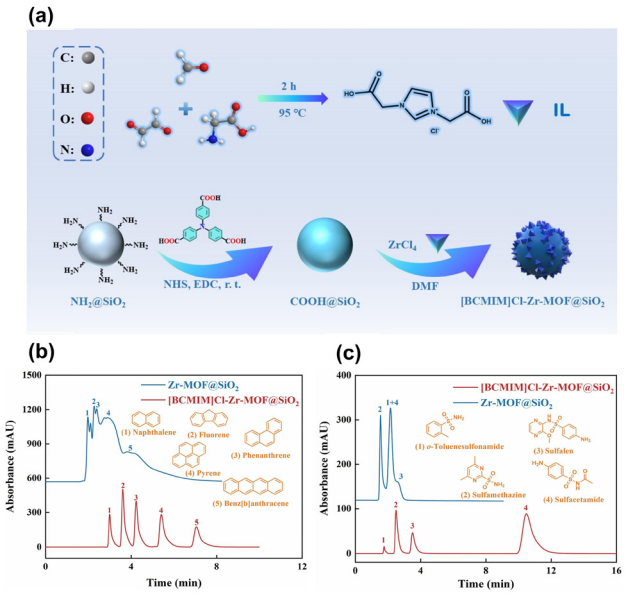

Fig. 3 (a) A synthetic scheme for the preparation of [BCMIM]Cl-Zr-MOF@SiO_2. Chromatograms of (b) PAHs and (c) sulfonamides on the [BCMIM]Cl-Zr-MOF@SiO_2 column and the Zr-MOF@SiO_2 column. Reproduced with permission from ref. 86. Copyright 2025, Elsevier.

3.2.1 3D carboxylate-based Zr-MOF coated columns. In 2012, Chang *et al.*[88] first developed the Zr-MOF, UiO-66, coated capillary column using the dynamic coating method. The UiO-66 coated column exhibited reverse shape selectivity for the separation of alkane isomers. The octahedral cavities of UiO-66 with pore windows measuring 7 Å permitted unrestricted access to all alkane isomers. The branched isomers with side methyl groups established closer contact with the cavity walls of UiO-66, while the linear isomers with the smallest molecular size experienced a relatively large free volume within the cavities of UiO-66. Consequently, as the degree of branching in alkane isomers increased, their interactions with UiO-66 strengthened, leading to prolonged retention time. Besides, the UiO-66 coated column provided both the reverse shape selectivity and molecular sieving effect for the separation of propylbenzene isomers. The elution order was 1,3,5-trimethylbenzene < *n*-propylbenzene < iso-propylbenzene, as the molecular size of 1,3,5-trimethylbenzene exceeded the window size of UiO-66 cavities. This steric hindrance restricted its diffusion into UiO-66 cavities, resulting in a shorter retention time and broader peak.

Subsequently, a lot of carboxylate-based Zr-MOFs have been used as GC stationary phases. Owing to the high tunability of Zr-MOFs, recent studies on their application as stationary phases in GC have focused on the precise modulation of their structural parameters, such as particle size, morphology, dimensionality, pore size, pore ratio, *etc*. Additionally, considerable efforts have been dedicated to elucidating the impact of these structural variations on chromatographic separation performance, aiming to optimize Zr-MOF-based stationary phases for enhanced GC separation efficiency.

The effect of particle size on the separation performance of Zr-MOF-based stationary phases was examined by Meng *et al.*[89] They synthesized both microscale and nanoscale variants of NU-1000, PCN-608, and PCN-222. Compared to their microscale counterparts, the nanoscale Zr-MOFs exhibited significantly improved separation performance (Fig. 4a). This improvement was attributed to the reduced mass transfer resistance of analytes within the nanoscale framework, while analytes encountered a higher diffusion barrier in the microscale Zr-MOFs. Thus, reducing the particle size could effectively shorten the diffusion path of analytes and lower diffusion resistance, thereby facilitating improved chromatographic separation performance.

In addition to particle size, the morphology of Zr-MOFs also plays a critical role in influencing separation behavior by altering the length of analyte diffusion pathways. Xu *et al.*[90] synthesized NU-901 with varying morphologies using water and monocarboxylic acid as modulators by adjusting their ratio. The resulting materials exhibited distinct stacking modes. Among them, NU-901-NP with tightly stacked pores demonstrated a more uniform pore size distribution and accelerated mass transfer, thereby enhancing separation efficiency. Subsequently, Xu *et al.*[91] developed the linker scissoring strat-

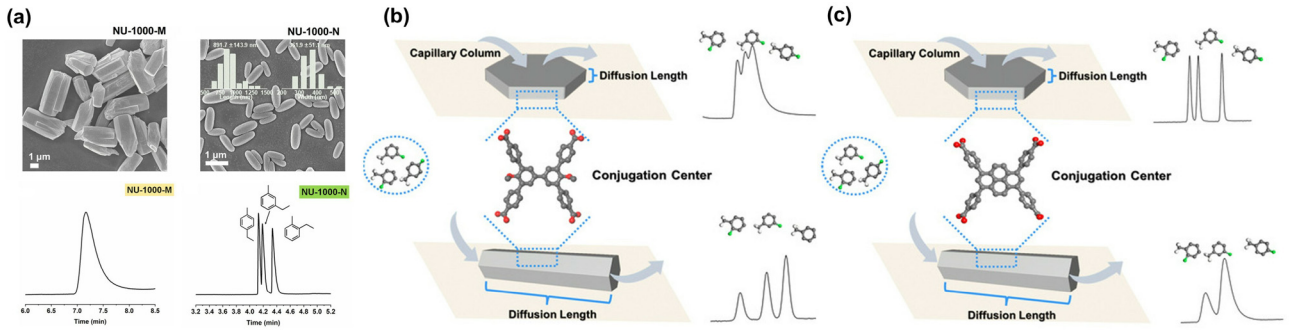

Fig. 4 (a) SEM and gas chromatograms of NU-1000-M and NU-1000-N. Reproduced with permission from ref. 89. Copyright 2022, American Chemical Society. Separation performance of (b) PCN-MOFs and (c) NU-MOFs influenced by both diffusion length and interaction centers. Reproduced with permission from ref. 91. Copyright 2022, John Wiley and Sons.

egy to synthesize PCN-608 and NU-1000 with distinct morphologies, including nanoplates (PCN-NPs and NU-NPs) and nanorods (PCN-NRs and NU-NRs), to illustrate the impact of morphology on chromatographic performance. When employed as stationary phases, PCN-NRs with longer diffusion pathways exhibited superior separation performance compared to PCN-NPs with shorter diffusion pathways. In contrast, NU-NPs outperformed NU-NRs. The opposite trends were attributed to differences in the interaction strengths between analytes and MOF structures. For PCN-MOFs, the relatively weak interactions provided by the channel walls required an extended diffusion pathway to adequately balance the thermodynamic interactions and the kinetic diffusion of analytes, thus favoring nanorod morphologies (Fig. 4b). In contrast, the large conjugate centers within linkers of NU-MOFs possessed strong thermodynamic interactions with analytes. In this case, shortening the diffusion path and reducing the diffusion resistance were more favorable for achieving optimal separation performance (Fig. 4c). These findings highlight that both structural and morphological modulations of Zr-MOFs are important in balancing the thermodynamic interactions and kinetic diffusion, thereby optimizing the chromatographic separation performance of Zr-MOFs.

Apart from the particle properties of Zr-MOFs, the pore size and the ratio of different pores in MOFs are also crucial determinants of their separation performance.[107] When the pore size is too small, analytes encounter high diffusion resistance and predominantly interact with the external surface of MOFs, leading to weak retention and potential co-elution. Conversely, when the pore size exceeds the molecular size of analytes, different analytes capable of diffusing into MOF pores are separated according to the strength of their thermodynamic interactions with the pore walls. However, excessively large pores promote rapid analyte diffusion, weakening the interactions and thereby reducing separation resolution. Therefore, precisely tuning the pore size or optimizing the ratio of different pores within MOFs can effectively regulate the diffusion behavior of analytes and affect the separation performance of MOFs.

Based on this, Xu *et al.*[92] developed a MOF solid solution (MOSS) strategy to homogeneously integrate NU-901 (***scu*** topology) and NU-1000 (***csq*** topology) structures into a single MOF nanocrystal. By adjusting the amount of bidentate ligand during synthesis, the micropore-to-mesopore ratio in MOSS was precisely controlled (Fig. 5a). The micropores in NU-901 facilitated specific interactions for the recognition and separation of analytes. However, the NU-901 coated column exhibited an obvious peak tailing phenomenon due to the high diffusion resistance. In contrast, a large number of mesopores in NU-1000 offered efficient diffusion pathways for rapid analyte transport, but the resulting insufficient interactions between analytes and pore walls led to poor separation ability of the NU-1000 coated column. All MOSS with different micropore-to-mesopore ratios exhibited improved separation abilities compared to the individual NU-901 and NU-1000, attributed to the balanced interplay between kinetic diffusion and thermodynamic interactions. Notably, MOSS-3, with the micropore-to-mesopore ratio of 1 : 1, achieved the best separation performance and unique selectivity, owing to an optimal balance between mass transfer efficiency and interaction strength (Fig. 5b and c).

Subsequently, Gao *et al.*[31] modulated the pore size of Zr-MOFs by incorporating two organic linkers of different lengths during the synthesis process. UiO-66 constructed with H_2BDC linkers possesses uniform micropores of approximately 1 nm, while DUT-52 constructed with 2,6-naphthalenedicarboxylic acid (H_2NDC) linkers features larger micropores of around 2 nm. By changing the ratio of BDC to NDC, Gao *et al.* synthesized continuously tunable Zr-MOFs (CTMOFs) exhibiting mixed structural features of both UiO-66 and DUT-52. As the H_2NDC content increased, the pore size of the CTMOF enhanced and the kinetic diffusion rate of analytes through CTMOFs progressively improved. For example, the diffusion rate of *m*X rose from 6.32×10^{-12} m^2 s^{-1} in CTMOF-1 to 1.55×10^{-11} m^2 s^{-1} in CTMOF-2 and 2.46×10^{-11} m^2 s^{-1} in CTMOF-3 (Fig. 5e). Notably, both excessively fast and slow mass transfer rates led to poor separation performance, whereas CTMOF-2 with a moderate mass transfer rate exhibited the best separation performance among other CTMOFs (Fig. 5d).

3.2.2 2D carboxylate-based Zr-MOF coated columns. Compared to 3D Zr-MOFs, 2D Zr-MOFs exhibit nanosheet

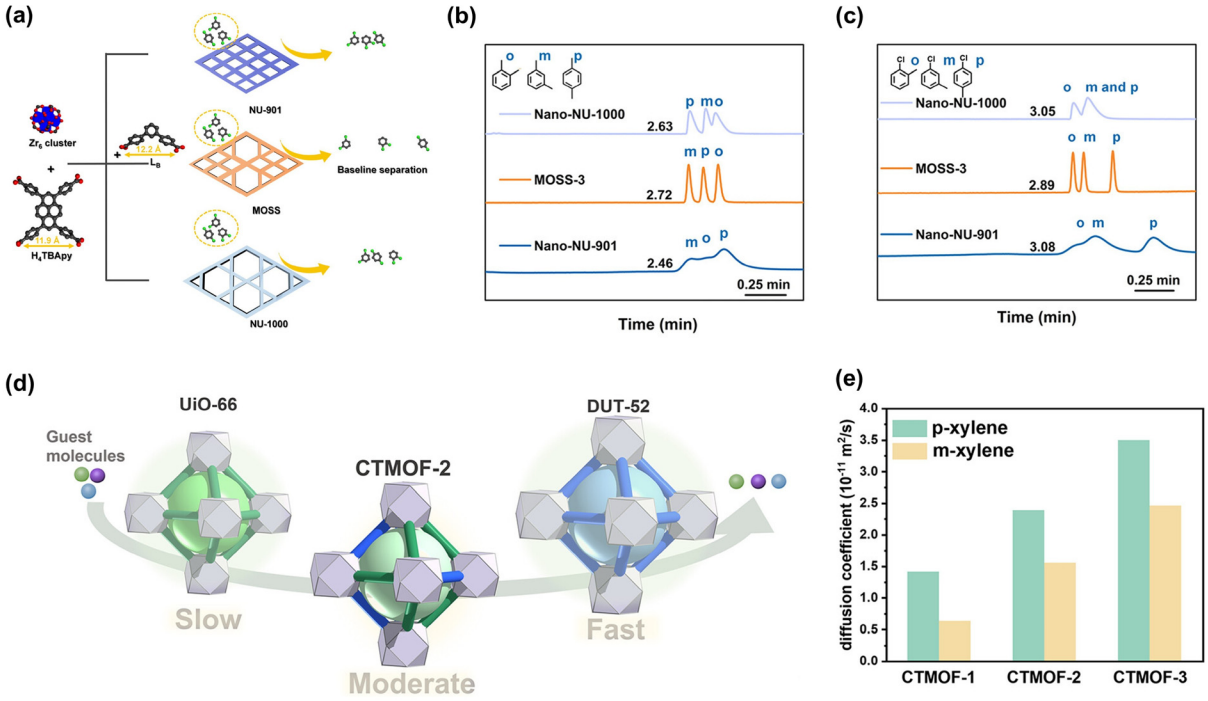

Fig. 5 (a) Schematic diagram of modulating the separation ability by the MOSS strategy. Gas chromatograms of (b) xylene and (c) chlorotoluene isomers on the MOSS-3, nano-NU-901, and nano-NU-1000 coated columns. Reproduced with permission from ref. 92. Copyright 2022, American Chemical Society. (d) Schematic diagram of analyte diffusion in UiO-66, DUT-52, and CTMOFs. (e) The diffusion coefficient for *p*-xylene and *m*-xylene on the CTMOF-1-, CTMOF-2-, and CTMOF-3 coated columns. Reproduced with permission from ref. 31. Copyright 2024, American Chemical Society.

structures that shorten the diffusion pathways of analytes and enable the formation of more uniform coatings within chromatographic columns, thereby minimizing column inhomogeneity. Yang *et al.*[93] investigated the influence of MOF structural dimensionality on GC separations by synthesizing UiO-67 frameworks with different dimensionalities including UiO-67-3D and UiO-67-2D. The UiO-67-3D contained two types of cavities with diameters of approximately 1.75 nm and 1.15 nm, respectively, which were interconnected by triangular windows (0.8 nm), while UiO-67-2D only featured the 0.8 nm triangular pores. The UiO-67-2D coated column demonstrated markedly enhanced separation capability and longer analyte retention time compared to the UiO-67-3D coated column. The presence of large cavities in UiO-67-3D caused overfast analyte diffusion and insufficient interactions, leading to weak retention and inferior separation. Conversely, without large cavities, UiO-67-2D restricted the analyte diffusion and increased the strength of interaction with analytes, which contributed to longer retention time and superior separation performance. In addition, Yang *et al.* also investigated the effect of nanosheet thickness in UiO-67-2D on chromatographic behavior. Among all MOFs, UiO-66-2D-2 with moderate thickness, achieved the highest separation efficiency due to the optimal diffusion length of analytes. This finding underscores the importance of controlling both dimensionality and morphological parameters, such as thickness, to optimize the chromatographic performance of 2D Zr-MOF-based stationary phases.

The stacking mode of 2D Zr-MOFs refers to the spatial arrangement of individual nanosheets within the assembled framework and plays a critical role in determining their structural properties and functional performance.[108] Depending on the synthetic conditions and interlayer interactions, 2D Zr-MOFs can adopt various stacking configurations, including eclipsed, staggered, or random stacking. These stacking modes significantly influence the interlayer spacing, accessible porosity, and the continuity of diffusion pathways. Tao *et al.*[94] pioneered the application of 2D Zr-BTB in GC and systematically investigated the impact of nanosheet stacking modes on separation performance (Fig. 6a). The twisted Zr-BTB-FA (FA = formic acid) nanosheets exhibited specific interlayer rotation angles of 8°, 14°, and 30°. Upon thermal treatment in ethanol, the twisted nanosheets were transformed into untwisted configurations (Fig. 6b). The ethanol molecules enabled the formation of Zr–O–Zr bonds between Zr_6 clusters in adjacent layers, thereby enforcing the untwisted stacking mode and generating highly ordered sub-nanometer pores. Chromatographic evaluations revealed that the twisted Zr-BTB-FA nanosheet coated column exhibited no separation ability for substituted benzene isomers. In contrast, the untwisted Zr-BTB-FA nanosheet coated column demonstrated high separation resolution for these isomers. The untwisted stacking produced highly uniform sub-nanometer pores that homogenized the diffusion pathway of analytes. This study highlights the critical importance of controlling stacking

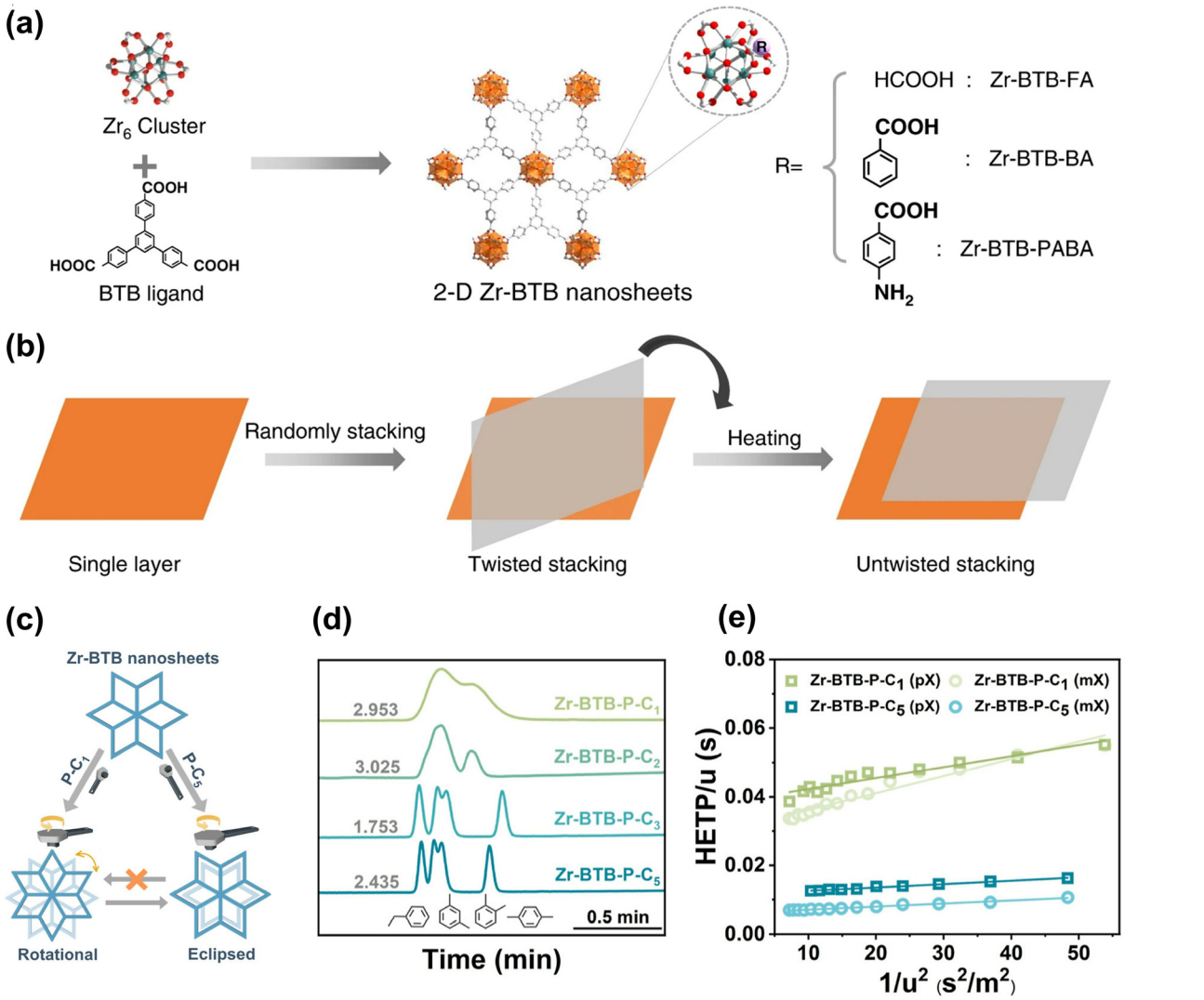

Fig. 6 (a) Synthesis of 2D Zr-BTB nanosheets with different acid modulators *via* coordination assembly of Zr_6 clusters and H_3BTB ligands. (b) Twisted and untwisted stacking modes of 2D Zr-BTB nanosheets. Reproduced with permission from ref. 94. Copyright 2019, Nature. (c) Schematic of modulating the stacking mode of 2D Zr-BTB nanosheets with phenyl-alkane acting as the "torque wrench". (d) Gas chromatogram of xylene isomers on these Zr-BTB-P coated columns. (e) Golay equation curves for *m*X and *p*X in Zr-BTB-P-C1 and Zr-BTB-P-C5 columns. Reproduced with permission from ref. 96. Copyright 2023, American Chemical Society.

modes in 2D Zr-MOFs to optimize their application as high-performance stationary phases in GC.

Tang *et al.*[95] employed solvent washing with different polarities to induce host–guest interactions and control the stacking modes of nanosheets. The untwisted stacked nanosheets with highly ordered pore structures achieved gas chromatographic separation of isomers. Building upon this foundation, Tang *et al.*[96] controlled the stacking mode of 2D Zr-BTB nanosheets by employing a series of bipolar solvent molecules with varying molecular sizes and polarities, which acted as "torque wrenches" (Fig. 6c). Toluene (P-C1), ethylbenzene (P-C2), propylbenzene (P-C3), and pentylbenzene (P-C5), containing identical polar phenyl groups but different alkyl chain lengths, induced distinct stacking modes of Zr-BTB nanosheets. As the alkyl chain length increased, the proportion of 0° eclipsed stacking increased from 48.2% in Zr-BTB-P-C1, 49.7% in Zr-BTB-P-C2 to 64.8% in Zr-BTB-P-C3, and 93.3% in Zr-BTB-P-C5. P-C1 and P-C2 provided multiple interactions such as hydrophobic and π–π interactions between adjacent nanosheets, favoring rational stacking. However, P-C3 and P-C5 were more likely to pass through rhombic nanochannels of Zr-BTB, enhancing the hydrophobic interactions along the inner pore walls and thus promoting predominantly eclipsed stacking (Fig. 6c). These stacking variations directly impacted gas chromatographic separation performance. The nanosheets with eclipsed stacking exhibited superior separation performance compared to rotational stacking nanosheets due to ordered and uniform pore structures, which enabled differential diffusion rates of isomers (Fig. 6d and e). A similar trend was observed when using acetate–alkane bipolar molecules (A-C2, A-C3, and A-C4)

to modulate the stacking modes of Zr-BTB nanosheets. Zr-BTB-A-C2 (50.4%) exhibited mainly rotational stacking, while Zr-BTB-A-C3 (79.6%) and Zr-BTB-A-C4 (76.0%) predominantly adopted eclipsed stacking. Correspondingly, the eclipsed Zr-BTB-A-C3 and Zr-BTB-A-C4 exhibited higher separation resolution than the rational Zr-BTB-A-C2, underscoring the critical role of ordered stacking and uniform nanopore structure in enhancing chromatographic performance.

Recently, Tang *et al.*[97] adjusted the wrinkling of Zr-BTB-Cx nanosheets by utilizing carboxylic acid modulators with different alkyl chain lengths, including formic acid (C1), ethanoic acid (C2), propionic acid (C3), butyric acid (C4), pentanoic acid (C5), and octanoic acid (C8). As the alkyl chain length increased, the surface hydrophobicity of the resulting nanosheets progressively increased from Zr-BTB-C1 to Zr-BTB-C8. This enhanced hydrophobicity weakened the interactions between Zr-BTB and the solvent, while simultaneously strengthening interlayer interactions among nanosheets. Such interlayer interactions induced mismatches that generated nanosheet wrinkling of varying degrees, thereby creating mesopores of different sizes. Appropriately sized mesopores could facilitate efficient mass transfer of analytes. However, excessively long alkyl chains may induce overly strong interlayer interactions, which suppress wrinkle formation and hinder mesopore generation. For GC separation, the Zr-BTB-C4 coated column exhibited the highest resolution in separating benzene isomers because the wrinkles of Zr-BTB-C4 brought an appropriate number and size of mesopores, which efficiently accelerated the mass transfer rate of analytes.

3.3 Application of carboxylate-based Zr-MOFs in CEC

CEC is a hybrid separation technique that synergistically combines the high selectivity of HPLC with the exceptional separation efficiency of capillary electrophoresis (CE). Utilizing the electroosmotic flow (EOF) as the driving force, CEC enables precise separation and analysis of analytes within capillary columns. There are three main types of CEC column configurations: particle-packed capillary columns, open-tubular capillary columns, and monolithic capillary columns.[109] Due to their simple fabrication process and resistance to clogging, open-tubular capillary columns are currently the main focus of both research and practical applications.[110]

In 2018, Tang *et al.*[98] reported an example of *in situ* growth of UiO-66-NH_2 on the inner wall of an open-tubular capillary for CEC application. Due to the synergistic effects of hydrophobic interactions, hydrogen bonding, π–π stacking, molecular sieving, and electrophoretic migration, the baseline separation of phenoxy acid, chlorobenzenes, and two groups of phenols was realized. However, most developed MOFs exhibit micrometer-scale dimensions and contain only micropores, resulting in severe diffusion limitations that restrict analytes access to internal interaction sites within the MOFs. To address this problem, Ji *et al.*[99] induced the synthesis of nanoscale hierarchical porous MOFs (NHP-MOFs) by adding regulators and pioneered their application as chromatographic stationary phases in capillary electrochromatographic separation. The incorporation of micropores and size reduction significantly accelerated molecular diffusion and mass transfer. The NHP-UiO-66 coated column had excellent resolution for substances such as chlorobenzene, substituted benzene, polycyclic aromatic hydrocarbons, nucleosides, peptides, and proteins. Compared with the UiO-66 coated column, it demonstrated enhanced separation performance (Fig. 7). To enable MOFs to rapidly crystallize *in situ* and adhere more uniformly and densely on the inner surface of capillaries, Ji *et al.*[100] developed a novel fabrication method utilizing a cysteine (Cys)-triggered *in situ* growth (ICISG) strategy to immobilize MOFs on capillaries. The resulting Cys-UiO-66@capillary exhibited marginally higher column efficiency for separating two aromatic compounds compared to previously reported UiO-66-modified columns. Subsequently, Liu *et al.*[101] fabricated Cys-UiO-66-NH_2@capillary through this method, which demonstrated exceptional separation capabilities for chlorobenzene isomers, selected alkaloids (*e.g.*, theobromine, theophylline), and nonsteroidal anti-inflammatory drugs (NSAIDs, *e.g.*, ketoprofen, ibuprofen). Leveraging its superior enzyme-loading capacity and high separation resolution, the Cys-UiO-66-NH_2@capillary was further functionalized with acetylcholinesterase (AChE) *via* electrostatic interactions, enabling CEC-based online enzymatic analysis.

In addition, chiral separation is also a key aspect of separation science. To achieve chiral separation ability, Ma *et al.*[102] used the condensation reaction between amino groups of UIO-66-NH_2 and carboxyl groups of cellulase to fabricate a chiral hybrid stationary phase. On the one hand, the abundant amino groups in UiO-66-NH_2 provided sites for anchoring chiral selectors. On the other hand, its abundant functional groups and inherent chiral recognition ability significantly enhanced the interaction with racemic analytes. Therefore, the obtained cellulase@poly(GMA-UiO-66-NH_2-EDMA) exhibited good separation for basic and acidic racemic drugs.

To reduce the risk of structural collapse during the grafting of the Zr-MOF on the matrix surface, Gao *et al.*[103] developed a novel chemically bonded open-tubular capillary column, L-Cys-PCN-224-bonded column, *via* a one-pot synthesis method. This approach successfully modified chiral ligand L(+)-cysteine (L-Cys) into the pores of PCN-224 (Fig. 8). This column achieved enantioseparation of nine amino acids, including acidic aspartic acid, neutral methionine, valine, leucine, phenylalanine, proline, glutamine, tryptophan, and basic histidine. Chiral recognition mostly relied on the steric complementarity between analytes and the chiral environment within the MOFs. Additional interactions, such as hydrogen bonding, π–π stacking, and electrostatic interactions, also contributed significantly to the separation mechanism.[111] Building on this strategy, Gao *et al.*[104] also prepared the L-Cys-PCN-222 bonded column. This column demonstrated efficient enantioseparation of 17 racemates, including acidic, neutral, and basic amino acids, as well as more complex compounds such as imidazolidinones and aryloxyphenoxypropionic acid herbicides.

Recently, Yan *et al.*[105] developed a novel nanomaterial synthesized from chiral molecularly imprinted polymers (CMIPs)

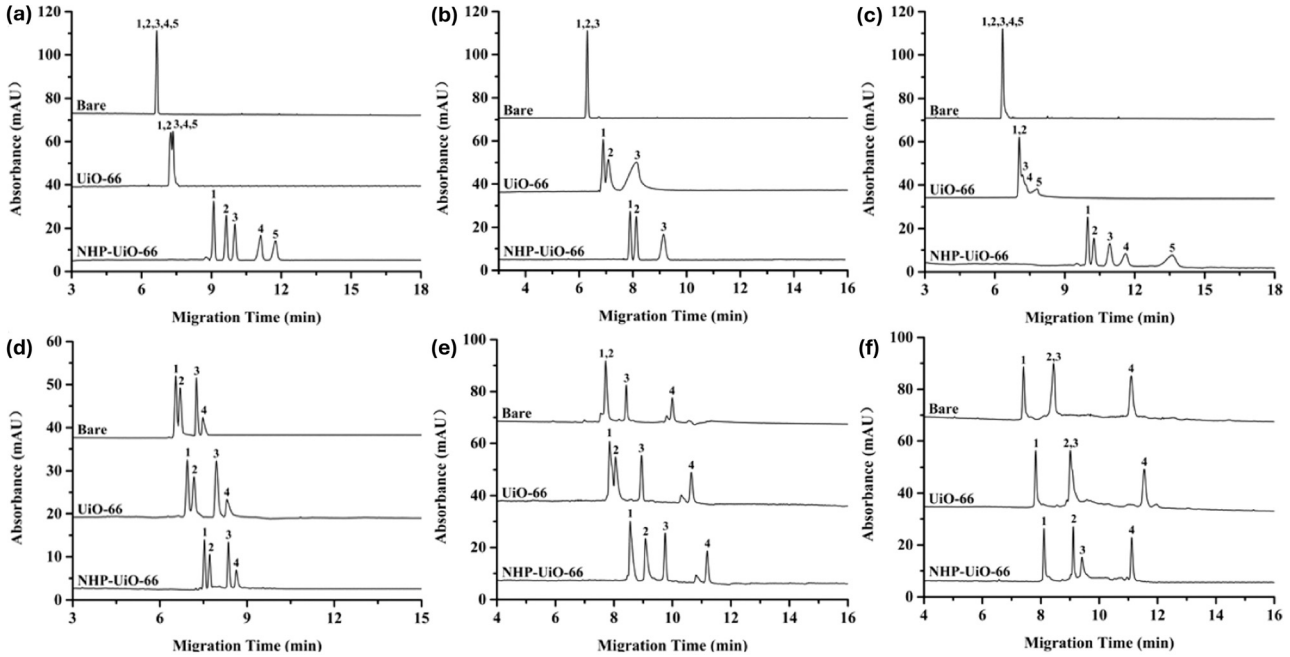

Fig. 7 Electropherograms of (a) substituted benzenes, (b) chlorobenzenes, (c) PAHs, (d) nucleosides, (e) polypeptides, (f) basic proteins on bare, UiO-66-coated, and HP-UiO-66-coated columns. Reproduced with permission from ref. 99. Copyright 2020, American Chemical Society.

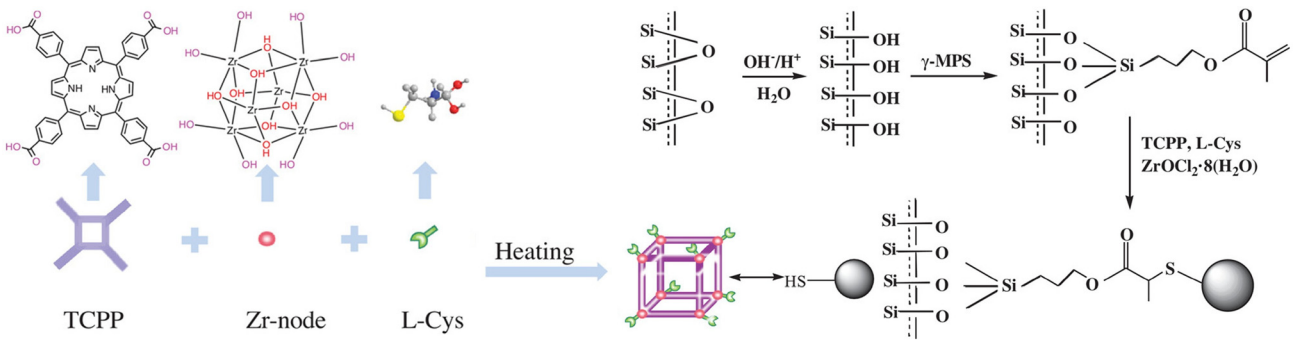

Fig. 8 Schematic illustration of the synthesis of L-Cys-PCN-224 and the preparation of the L-Cys-PCN-224-bonded open-tubular column. Reproduced with permission from ref. 103. Copyright 2022, John Wiley and Sons.

and achiral MOFs. The imprinted cavities of CMIPs exhibited a memory effect towards template molecules, enabling specific recognition of structurally similar targets. By integrating MOFs with CMIPs as chromatographic stationary phases, the loading capacity of CMIPs on the achiral MOF stationary phases was enhanced. Moreover, the inherent rigidity of MOFs mechanically supported the imprinted cavities, preventing structural deformation and thereby improving separation selectivity and efficiency. Experimental results demonstrated that the composite material L-tryptophan (L-TRP)@MIP(APTES-TEOS)@UiO-66-NH_2@capillary achieved chiral separation of DL-TRP successfully. In contrast, the non-imprinted polymer composite NIP(APTES-TEOS)@UiO-66-NH_2@capillary, L-TRP@MIP(APTES-TEOS)@capillary and the UiO-66-NH_2@capillary all showed no chiral separation ability on DL-TRP.

4. Conclusion and outlook

In summary, this review has provided a comprehensive overview of the classification of Zr-MOFs and their applications as stationary phases in chromatographic separations. Owing to their excellent thermal, chemical, and mechanical stability, Zr-MOFs can be effectively packed or coated into chromatographic columns while retaining their structural integrity and functional properties. Furthermore, the diverse coordination modes between Zr clusters and organic linkers give rise to various topological structures, thereby offering significant potential for the utilization of chromatographic stationary phases. Nevertheless, the direct use of pristine Zr-MOFs as chromatographic stationary phases still presents certain challenges, underscoring the need for structural

modification to broaden their practical applicability. Structural modulation of Zr-MOFs focuses on controlling the pore size, pore shape, and surface microenvironment to improve selectivity and meet specific chromatographic separation requirements. Ligand design enables tailored adjustment of Zr-MOF topology, pore size, and channel dimensionality by selecting linkers with specific functional groups or geometries. Post-synthetic modification fine-tunes pore surface chemistry through grafting functional groups (*e.g.*, polar groups, chiral sites) onto the framework, while defect engineering effectively modulates local microenvironments, porosity, and channel tortuosity. These modifications optimize thermodynamic interactions between the Zr-MOF and analytes, as well as analyte diffusion within the framework, thereby significantly enhancing chromatographic separation selectivity and resolution. For gas chromatography applications, simultaneous optimization of particle size and porosity is also essential to ensure efficient mass transfer of analytes. In liquid chromatography, the Zr-MOF composites exhibit synergistic effects in that the Zr-MOF composite packed column not only mitigates the high backpressure but also allows for fine-tuning of pore architecture through the rational design of MOF structures or silica spheres. As a result, both the analyte mass transfer and column efficiency can be improved. However, current research remains predominantly focused on classical Zr-MOF systems, such as UiO-66, and many performance enhancement strategies only rely on stringent structural or chemical design criteria. Therefore, future research should prioritize the development of novel Zr-MOF-based stationary phases and the establishment of universal and versatile framework modification methodologies, enabling precise tailoring of separation performance across a broader spectrum of analytes and separation techniques.

Author contributions

H.-Y. W.: investigation, formal analysis, and writing – original draft; S.-S. M.: validation, formal analysis, and writing – review and editing; J. Z.: investigation; M.-H. G.: validation; M. X.: project administration, funding acquisition, and writing – review and editing; and Z.-Y. G.: project administration, funding acquisition, and writing – review and editing.

Conflicts of interest

There are no conflicts to declare.

Data availability

No primary research results, software, or code have been included and no new data were generated or analyzed as part of this review.

Acknowledgements

This work is supported by the National Natural Science Foundation of China (22174067, 22204078, 22374077, and 22474059), the Natural Science Foundation of Jiangsu Province of China (BK20220370), the Jiangsu Association for Science and Technology (TJ-2023-076), and the Priority Academic Program Development of Jiangsu Higher Education Institutions.

References

1 Y. Xu, A. K. Rashwan, A. I. Osman, E. M. Abd El-Monaem, A. M. Elgarahy, A. S. Eltaweil, M. Omar, Y. Li, A.-H. E. Mehanni, W. Chen and D. W. Rooney, *Environ. Chem. Lett.*, 2023, **21**, 447–477.
2 N. Manousi, G. A. Zachariadis and E. A. Deliyanni, *Environ. Sci. Pollut. Res.*, 2021, **28**, 59015–59039.
3 C. Liu, C. Tian, J. Guo, X. Zhang, L. Wu, L. Zhu and B. Du, *ACS Appl. Mater. Interfaces*, 2024, **16**, 43156–43170.
4 Q. Yu, Q. Zhang, Z. Wu and Y. Yang, *ACS Nano*, 2025, **19**, 3037–3053.
5 X. Wang, X. Ma, H. Wang, P. Huang, X. Du and X. Lu, *Microchim. Acta*, 2017, **184**, 3681–3687.
6 Y. Wu, X. Wang, K. O. Kirlikovali, X. Gong, A. Atilgan, K. Ma, N. M. Schweitzer, N. C. Gianneschi, Z. Li, X. Zhang and O. K. Farha, *Angew. Chem., Int. Ed.*, 2022, **61**, e202117528.
7 B. Wang, W. Li, J. Liu, T. Gan, S. Gao, L. Li, T. Zhang, Y. Zhou, Z. Shi, J. Li, Y. Liu and J. Yu, *Adv. Mater.*, 2025, 2407154.
8 H. Yang, J. Zheng, W. Wang, J. Lin, J. Wang, L. Liu, W. Wu, C. Zhang, M. Zhang, Y. Fu, B. Yang and Y. Liao, *Adv. Sci.*, 2024, **11**, 2405848.
9 F. Lang, L. Zhang, Y. Li, X.-J. Xi, J. Pang, W. Zheng, H.-C. Zhou and X.-H. Bu, *Angew. Chem., Int. Ed.*, 2025, **64**, e202422517.
10 R. Chen, B. Sheng, F. Zheng, J. Li, H. Sun, F. Zhou, L. Chen, Z. Zhang, Q. Yang, Q. Ren and Z. Bao, *AIChE J.*, 2023, **69**, e18169.
11 Y. Sun, J. Yan, Y. Gao, T. Ji, S. Chen, C. Wang, P. Lu, Y. Li and Y. Liu, *Angew. Chem., Int. Ed.*, 2023, **62**, e202216697.
12 S. Ma, L. Shi, Y. Zhong, H. Cao, Z. Yang, J. Yang, K. Wang and Z. Chen, *Small*, 2025, **21**, 2409138.
13 W. Gong, Y. Xie, A. Yamano, S. Ito, X. Tang, E. W. Reinheimer, C. D. Malliakas, J. Dong, Y. Cui and O. K. Farha, *J. Am. Chem. Soc.*, 2023, **145**, 26890–26899.
14 O. M. Yaghi, M. O'Keeffe, N. W. Ockwig, H. K. Chae, M. Eddaoudi and J. Kim, *Nature*, 2003, **423**, 705–714.
15 Z. Chen, K. O. Kirlikovali, P. Li and O. K. Farha, *Acc. Chem. Res.*, 2022, **55**, 579–591.
16 S. Yuan, P. Zhang, L. Zhang, A. T. Garcia-Esparza, D. Sokaras, J.-S. Qin, L. Feng, G. S. Day, W. Chen, H. F. Drake, P. Elumalai, S. T. Madrahimov, D. Sun and H.-C. Zhou, *J. Am. Chem. Soc.*, 2018, **140**, 10814–10819.

17 K. K. Tanabe and S. M. Cohen, *Chem. Soc. Rev.*, 2011, **40**, 498–519.
18 Y. Bai, Y. Dou, L.-H. Xie, W. Rutledge, J.-R. Li and H.-C. Zhou, *Chem. Soc. Rev.*, 2016, **45**, 2327–2367.
19 S. Wang, J. Wang, W. Cheng, X. Yang, Z. Zhang, Y. Xu, H. Liu, Y. Wu and M. Fang, *Dalton Trans.*, 2015, **44**, 8049–8061.
20 J. H. Cavka, S. Jakobsen, U. Olsbye, N. Guillou, C. Lamberti, S. Bordiga and K. P. Lillerud, *J. Am. Chem. Soc.*, 2008, **130**, 13850–13851.
21 W. Morris, B. Volosskiy, S. Demir, F. Gándara, P. L. McGrier, H. Furukawa, D. Cascio, J. F. Stoddart and O. M. Yaghi, *Inorg. Chem.*, 2012, **51**, 6443–6445.
22 V. Bon, V. Senkovskyy, I. Senkovska and S. Kaskel, *Chem. Commun.*, 2012, **48**, 8407–8409.
23 H. Furukawa, F. Gándara, Y.-B. Zhang, J. Jiang, W. L. Queen, M. R. Hudson and O. M. Yaghi, *J. Am. Chem. Soc.*, 2014, **136**, 4369–4381.
24 J. E. Mondloch, W. Bury, D. Fairen-Jimenez, S. Kwon, E. J. DeMarco, M. H. Weston, A. A. Sarjeant, S. T. Nguyen, P. C. Stair, R. Q. Snurr, O. K. Farha and J. T. Hupp, *J. Am. Chem. Soc.*, 2013, **135**, 10294–10297.
25 S.-S. Meng, M. Xu, H. Guan, C. Chen, P. Cai, B. Dong, W.-S. Tan, Y.-H. Gu, W.-Q. Tang, L.-G. Xie, S. Yuan, Y. Han, X. Kong and Z.-Y. Gu, *Nat. Commun.*, 2023, **14**, 5347.
26 L. Shi, Z. Yang, F. Sha and Z. Chen, *Sci. China Chem.*, 2023, **66**, 3383–3397.
27 C. Zhang, F. Formalik, D. Lv, F. Sha, K. O. Kirlikovali, X. Wang, X. Tang, S. Su, H. Xie, Y. Chen, Z. Li, R. Q. Snurr and O. K. Farha, *Angew. Chem., Int. Ed.*, 2025, **64**, e202424260.
28 K. O. Kirlikovali, Z. Chen, T. Islamoglu, J. T. Hupp and O. K. Farha, *ACS Appl. Mater. Interfaces*, 2020, **12**, 14702–14720.
29 Y. Geng, Y. Gao, P. Gao, J. Zhang, X. Tang, J. Dong, J. Jiao, H. Niu, W. Gong and Y. Cui, *J. Am. Chem. Soc.*, 2025, **147**, 7663–7670.
30 X. Na, S. Xing, M. Tan and W. Su, *Adv. Sci.*, 2024, **11**, 2409451.
31 Y.-X. Gao, X.-N. Yi, Z.-C. Tang, H. Yang, W. Wang, M. Xu and Z.-Y. Gu, *Anal. Chem.*, 2024, **96**, 6476–6482.
32 P. Hu, J. Han, J. Zhou, H. Wang, C. Xiong, H. Liu, X. Zhou, Y. Wang and H. Ji, *Chem. Eng. J.*, 2021, **426**, 131302.
33 P. S. Bárcia, D. Guimarães, P. A. P. Mendes, J. A. C. Silva, V. Guillerm, H. Chevreau, C. Serre and A. E. Rodrigues, *Microporous Mesoporous Mater.*, 2011, **139**, 67–73.
34 G. C. Shearer, S. Chavan, S. Bordiga, S. Svelle, U. Olsbye and K. P. Lillerud, *Chem. Mater.*, 2016, **28**, 3749–3761.
35 A. Jrad, G. Al Sabeh, K. Hannouche, R. Al Natour, O. Haidar, H. Sammoury, M. N. Ahmad and M. Hmadeh, *ACS Appl. Nano Mater.*, 2023, **6**, 18698–18720.
36 A. Jrad, M. Hmadeh, B. J. Abu Tarboush, G. Awada and M. Ahmad, *Chem. Eng. J.*, 2020, **382**, 122793.
37 S. Dissegna, R. Hardian, K. Epp, G. Kieslich, M.-V. Coulet, P. Llewellyn and R. A. Fischer, *CrystEngComm*, 2017, **19**, 4137–4141.
38 G. Cai and H.-L. Jiang, *Angew. Chem., Int. Ed.*, 2017, **56**, 563–567.
39 A. Schaate, P. Roy, A. Godt, J. Lippke, F. Waltz, M. Wiebcke and P. Behrens, *Chem. Eur. J.*, 2011, **17**, 6643–6651.
40 D. Feng, Z.-Y. Gu, J.-R. Li, H.-L. Jiang, Z. Wei and H.-C. Zhou, *Angew. Chem., Int. Ed.*, 2012, **51**, 10307–10310.
41 P.-H. Chang, R. Mukhopadhyay, B. Zhong, Q.-Y. Yang, S. Zhou, Y.-M. Tzou and B. Sarkar, *J. Colloid Interface Sci.*, 2023, **636**, 459–469.
42 H. Li, X. Cao, C. Zhang, Q. Yu, Z. Zhao, X. Niu, X. Sun, Y. Liu, L. Ma and Z. Li, *RSC Adv.*, 2017, **7**, 16273–16281.
43 C. Bi, C. Zhang, W. Xu, F. Ma, L. Zhu, R. Zhu, Q. Qi, L. Liu, J. Bai and H. Dong, *Desalination*, 2023, **545**, 116169.
44 X. Zhao, H. Zhao, W. Dai, Y. Wei, Y. Wang, Y. Zhang, L. Zhi, H. Huang and Z. Gao, *J. Colloid Interface Sci.*, 2018, **526**, 28–34.
45 Y. Liang, X. Yang, X. Wang, Z.-J. Guan, H. Xing and Y. Fang, *Nat. Commun.*, 2023, **14**, 5223.
46 R. Abazari, S. Sanati, M. A. Bajaber, M. S. Javed, P. C. Junk, A. K. Nanjundan, J. Qian and D. P. Dubal, *Small*, 2024, **20**, 2306353.
47 D. Ray, S. Goswami, J. Duan, J. T. Hupp, C. J. Cramer and L. Gagliardi, *Chem. Mater.*, 2021, **33**, 1182–1189.
48 R. Wang, B. C. Bukowski, J. Duan, J. Sui, R. Q. Snurr and J. T. Hupp, *Chem. Mater.*, 2021, **33**, 6832–6840.
49 T. E. Webber, W.-G. Liu, S. P. Desai, C. C. Lu, D. G. Truhlar and R. L. Penn, *ACS Appl. Mater. Interfaces*, 2017, **9**, 39342–39346.
50 S. J. Garibay, I. Iordanov, T. Islamoglu, J. B. DeCoste and O. K. Farha, *CrystEngComm*, 2018, **20**, 7066–7070.
51 S. Gorla, M. L. Díaz-Ramírez, N. S. Abeynayake, D. M. Kaphan, D. R. Williams, V. Martis, H. A. Lara-García, B. Donnadieu, N. Lopez, I. A. Ibarra and V. Montiel-Palma, *ACS Appl. Mater. Interfaces*, 2020, **12**, 41758–41764.
52 P. K. Verma, C. A. Koellner, H. Hall, M. R. Phister, K. H. Stone, A. W. Nichols, A. Dhakal, E. Ashcraft, C. W. Machan and G. Giri, *ACS Appl. Mater. Interfaces*, 2023, **15**, 53913–53923.
53 Z. Li, N. M. Schweitzer, A. B. League, V. Bernales, A. W. Peters, A. B. Getsoian, T. C. Wang, J. T. Miller, A. Vjunov, J. L. Fulton, J. A. Lercher, C. J. Cramer, L. Gagliardi, J. T. Hupp and O. K. Farha, *J. Am. Chem. Soc.*, 2016, **138**, 1977–1982.
54 N. Klein, C. Herzog, M. Sabo, I. Senkovska, J. Getzschmann, S. Paasch, M. R. Lohe, E. Brunner and S. Kaskel, *Phys. Chem. Chem. Phys.*, 2010, **12**, 11778–11784.
55 V. Bon, I. Senkovska, I. A. Baburin and S. Kaskel, *Cryst. Growth Des.*, 2013, **13**, 1231–1237.
56 A. G. Attallah, V. Bon, K. Maity, E. Hirschmann, M. Butterling, A. Wagner and S. Kaskel, *ACS Appl. Mater. Interfaces*, 2023, **15**, 48264–48276.
57 Y. Wang, H. Chen, Z. Liu, J. Li, Z. Tu and S. Li, *Microporous Mesoporous Mater.*, 2023, **354**, 112554.

58 S. Xiao, M. Li, H. Cong, L. Wang, X. Li and W. Zhang, *Polymers*, 2021, **13**, 4075.
59 X. Chen, S. Xie, G. Wang, H. Liu, Y. Guo, S. Yang, S. Wu and X. Liu, *J. Radioanal. Nucl. Chem.*, 2021, **328**, 181–194.
60 T. Wang, A. Hu, G. Xu, C. Liu, H. Wang and Y. Xia, *Catal. Lett.*, 2019, **149**, 1845–1855.
61 Y. Lin, Y. Li, Y. Cao and X. Wang, *Chem. – Asian J.*, 2021, **16**, 3281–3298.
62 W. Wang, Y. Yu, Y. Jin, X. Liu, M. Shang, X. Zheng, T. Liu and Z. Xie, *J. Nanobiotechnol.*, 2022, **20**, 207.
63 Z. Deng, T. Wan, D. Chen, W. Ying, Y.-J. Zeng, Y. Yan and X. Peng, *Small*, 2020, **16**, 2002699.
64 D. Zhang, X.-N. Zou, X.-G. Wang, J. Su, T.-X. Luan, W. Fan, P.-Z. Li and Y. Zhao, *ACS Appl. Mater. Interfaces*, 2022, **14**, 23518–23526.
65 Y. Wang, M. Zhao, J. Ping, B. Chen, X. Cao, Y. Huang, C. Tan, Q. Ma, S. Wu, Y. Yu, Q. Lu, J. Chen, W. Zhao, Y. Ying and H. Zhang, *Adv. Mater.*, 2016, **28**, 4149–4155.
66 Y. Cheng, W.-Q. Tang, L.-T. Geng, M. Xu, J.-P. Zhu, S.-S. Meng and Z.-Y. Gu, *Chem. Sci.*, 2024, **15**, 4106–4113.
67 R. Wang, Z. Wang, Y. Xu, F. Dai, L. Zhang and D. Sun, *Inorg. Chem.*, 2014, **53**, 7086–7088.
68 Z. Hu, E. M. Mahdi, Y. Peng, Y. Qian, B. Zhang, N. Yan, D. Yuan, J.-C. Tan and D. Zhao, *J. Mater. Chem. A*, 2017, **5**, 8954–8963.
69 Y. Wang, L. Feng, J. Pang, J. Li, N. Huang, G. S. Day, L. Cheng, H. F. Drake, Y. Wang, C. Lollar, J. Qin, Z. Gu, T. Lu, S. Yuan and H.-C. Zhou, *Adv. Sci.*, 2019, **6**, 1802059.
70 J. Zhang and Z. Chen, *J. Chromatogr. A*, 2017, **1530**, 1–18.
71 K. Yusuf, A. Aqel and Z. Alothman, *J. Chromatogr. A*, 2014, **1348**, 1–16.
72 H. Zhang, P. Xiong, G. Li, C. Liao and G. Jiang, *TrAC Trends Anal. Chem.*, 2020, **131**, 116015.
73 W.-W. Zhao, C.-Y. Zhang, Z.-G. Yan, L.-P. Bai, X. Wang, H. Huang, Y.-Y. Zhou, Y. Xie, F.-S. Li and J.-R. Li, *J. Chromatogr. A*, 2014, **1370**, 121–128.
74 L. Alaerts, C. E. A. Kirschhock, M. Maes, M. A. van der Veen, V. Finsy, A. Depla, J. A. Martens, G. V. Baron, P. A. Jacobs, J. F. M. Denayer and D. E. De Vos, *Angew. Chem., Int. Ed.*, 2007, **46**, 4293–4297.
75 L. Alaerts, M. Maes, L. Giebeler, P. A. Jacobs, J. A. Martens, J. F. M. Denayer, C. E. A. Kirschhock and D. E. De Vos, *J. Am. Chem. Soc.*, 2008, **130**, 14170–14178.
76 S. Chen, X.-X. Li, F. Feng, S. Li, J.-H. Han, Z.-Y. Jia, L. Shu, P. Somsundaran and J.-R. Li, *J. Sep. Sci.*, 2018, **41**, 2528–2535.
77 T. Si, J. Ma, X. Lu, L. Wang, X. Liang and S. Wang, *ACS Appl. Nano Mater.*, 2020, **3**, 351–356.
78 X. Zhang, Q. Han and M. Ding, *RSC Adv.*, 2015, **5**, 1043–1050.
79 X. Li, B. Li, M. Liu, Y. Zhou, L. Zhang and X. Qiao, *ACS Appl. Mater. Interfaces*, 2019, **11**, 10320–10327.
80 Z. Hu, J. Liao, J. Zhou, L. Zhao, Y. Liu, Y. Zhang, W. Chen and S. Tang, *Chin. Chem. Lett.*, 2025, **36**, 109985.
81 R. D. Arrua, A. Peristyy, P. N. Nesterenko, A. Das, D. M. D'Alessandro and E. F. Hilder, *Analyst*, 2017, **142**, 517–524.
82 J. Wang, Y. He, X. Wan, F. Xie, Y. Sun, T. Li, Q. Xu, D. Zhao and Q. Qu, *J. Chromatogr. A*, 2023, **1705**, 464164.
83 H. Jiang, K. Yang, X. Zhao, W. Zhang, Y. Liu, J. Jiang and Y. Cui, *J. Am. Chem. Soc.*, 2021, **143**, 390–398.
84 T. Si, X. Lu, H. Zhang, X. Liang, S. Wang and Y. Guo, *Microchim. Acta*, 2021, **188**, 360.
85 T. Si, J. Zhao, J. Li, G. Zhang, S. Wang, Y. Guo, X. Liang, Y. Yang and R. Rong, *Microchem. J.*, 2024, **205**, 111339.
86 J. Zhou, Y. Liu, Y. Zhang, W. Chen and S. Tang, *Sep. Purif. Technol.*, 2025, **354**, 128718.
87 W. Zhang, Z. Ke, Y. Liu, J. Xiong, W. Chen and S. Tang, *Sep. Purif. Technol.*, 2025, **369**, 133126.
88 N. Chang and X.-P. Yan, *J. Chromatogr. A*, 2012, **1257**, 116–124.
89 S.-S. Meng, T. Han, Y.-H. Gu, C. Zeng, W.-Q. Tang, M. Xu and Z.-Y. Gu, *Anal. Chem.*, 2022, **94**, 14251–14256.
90 M. Xu, S.-S. Meng, P. Cai, W.-Q. Tang, Y.-D. Yin, J. A. Powell, H.-C. Zhou and Z.-Y. Gu, *Chem. Sci.*, 2021, **12**, 4104–4110.
91 M. Xu, P. Cai, S.-S. Meng, Y. Yang, D.-S. Zheng, Q.-H. Zhang, L. Gu, H.-C. Zhou and Z.-Y. Gu, *Angew. Chem., Int. Ed.*, 2022, **61**, e202207786.
92 M. Xu, S.-S. Meng, P. Cai, Y.-H. Gu, T.-A. Yan, T.-H. Yan, Q.-H. Zhang, L. Gu, D.-H. Liu, H.-C. Zhou and Z.-Y. Gu, *ACS Cent. Sci.*, 2022, **8**, 184–191.
93 H. Yang, J.-J. Liu, W.-Q. Tang, S.-S. Meng, Y.-X. Gao, W. Li, H. Zhang, M. Xu and Z.-Y. Gu, *Anal. Chem.*, 2023, **95**, 18760–18766.
94 Z.-R. Tao, J.-X. Wu, Y.-J. Zhao, M. Xu, W.-Q. Tang, Q.-H. Zhang, L. Gu, D.-H. Liu and Z.-Y. Gu, *Nat. Commun.*, 2019, **10**, 2911.
95 W.-Q. Tang, Y.-J. Zhao, M. Xu, J.-Y. Xu, S.-S. Meng, Y.-D. Yin, Q.-H. Zhang, L. Gu, D.-H. Liu and Z.-Y. Gu, *Angew. Chem., Int. Ed.*, 2021, **60**, 6920–6925.
96 W.-Q. Tang, X. Yi, H. Guan, X.-W. Wang, Y.-W. Gu, Y.-J. Zhao, J. Fu, W. Li, Y. Cheng, S.-S. Meng, M. Xu, Q.-H. Zhang, L. Gu, X. Kong, D.-H. Liu, W. Wang and Z.-Y. Gu, *J. Am. Chem. Soc.*, 2023, **145**, 26580–26591.
97 W.-Q. Tang, Y. Cheng, J.-P. Zhu, Y.-Q. Zhou, M. Xu and Z.-Y. Gu, *Angew. Chem., Int. Ed.*, 2024, **63**, e202409588.
98 P. Tang, R. Wang and Z. Chen, *Electrophoresis*, 2018, **39**, 2619–2625.
99 B. Ji, G. Yi, K. Zhang, Y. Zhang, Y. Gui, D. Gao, J. Zeng, L. Wang, Z. Xia and Q. Fu, *Anal. Chem.*, 2020, **92**, 15655–15662.
100 B. Ji, G. Yi, Y. Gui, J. Zhang, W. Long, M. You, Z. Xia and Q. Fu, *ACS Appl. Mater. Interfaces*, 2021, **13**, 41075–41083.
101 R. Liu, G. Yi, B. Ji, X. Liu, Y. Gui, Z. Xia and Q. Fu, *Anal. Chem.*, 2022, **94**, 6540–6547.
102 M. Ma, J. Zhang, P. Li, Y. Du, J. Gan, J. Yang and L. Zhang, *Microchim. Acta*, 2021, **188**, 186.
103 L. Gao, X. Hu, S. Qin, H. Chu, Y. Tang, X. Li and B. Wang, *Electrophoresis*, 2022, **43**, 1161–1173.

104 L. Gao, X. Hu, S. Qin, H. Chu, X. Zhao and B. Wang, *RSC Adv.*, 2022, **12**, 6063–6075.
105 Y. Yan, P. Miao, S. Du and Y. Du, *Microchim. Acta*, 2025, **192**, 170.
106 X.-Y. Yang, L. Gao, Y.-M. Sun, W.-J. Zhao, G.-Q. Xiang, X.-M. Jiang, L.-J. He and S.-S. Zhang, *Chin. J. Anal. Chem.*, 2020, **48**, 1607–1615.
107 X.-J. Xie, M.-Y. Zhou, H. Zeng, W. Lu and D. Li, *Acc. Mater. Res.*, 2025, **6**, 195–209.
108 W. Wu, X. Cai, X. Yang, Y. Wei, L. Ding, L. Li and H. Wang, *Nat. Commun.*, 2024, **15**, 10730.
109 S. Declerck, Y. Vander Heyden and D. Mangelings, *J. Pharm. Biomed.*, 2016, **130**, 81–99.
110 L.-F. Hu, S.-J. Yin, H. Zhang and F.-Q. Yang, *J. Sep. Sci.*, 2020, **43**, 1942–1966.
111 R. Krishna and J. M. van Baten, *Sep. Purif. Technol.*, 2007, **55**, 246–255.